

Dartmouth College

## Dartmouth Digital Commons

---

Dartmouth College Undergraduate Theses

Theses and Dissertations

---

6-1-1999

# Improved Computer Detection and Mapping of Cerebral Oxygenation

David H. Kung  
*Dartmouth College*

Follow this and additional works at: [https://digitalcommons.dartmouth.edu/senior\\_theses](https://digitalcommons.dartmouth.edu/senior_theses)



Part of the [Computer Sciences Commons](#)

---

### Recommended Citation

Kung, David H., "Improved Computer Detection and Mapping of Cerebral Oxygenation" (1999). *Dartmouth College Undergraduate Theses*. 195.

[https://digitalcommons.dartmouth.edu/senior\\_theses/195](https://digitalcommons.dartmouth.edu/senior_theses/195)

This Thesis (Undergraduate) is brought to you for free and open access by the Theses and Dissertations at Dartmouth Digital Commons. It has been accepted for inclusion in Dartmouth College Undergraduate Theses by an authorized administrator of Dartmouth Digital Commons. For more information, please contact [dartmouthdigitalcommons@groups.dartmouth.edu](mailto:dartmouthdigitalcommons@groups.dartmouth.edu).

# Improved Computer Detection and Mapping of Cerebral Oxygenation

*David Kung*

Advisors: George Cybenko, Keith Paulsen, Brian Pogue

Senior Honors Thesis in Computer Science modified with Engineering

Computer Science Technical Report PCS-TR99-349

Dartmouth College

Hanover, NH 03755

Spring, 1999

## **Abstract**

Near-infrared (NIR) optical image reconstruction that incorporates blood oxygen level dependant (BOLD) magnetic resonance imaging has the potential to improve both quantifiable measurement of oxygenation and the spatial resolution involved in such mapping. My thesis continues some preliminary work in this area through development of an analytic diffusion parameter estimation algorithm for use with a NIR imaging array and development of a finite element mesh utility to read *a priori* BOLD images and tag them with property elements for NIR image resolution improvement.

## **1 Introduction**

Oxygen is a required substrate for the brain but currently there is no acceptable method for accurately monitoring and mapping cerebral oxygenation. Many disorders widespread in incidence are attributed to affected cerebral oxygenation. For example, pre-term infants are especially at risk for abnormalities associated with underdeveloped vasculature which limits the supply of oxygen and nutrients to the brain during the first few weeks after birth. Stroke patients also have a complex relationship between oxygenation both during and after the infarct and survival and would similarly benefit from a non-invasive method of spatially and temporally accurate monitoring. A variety of studies have indicated that oxygenation may change during normal brain function, increasing during task activation, which may be useful in mapping associated brain function (Bandettini et al., 1992; Kwong et al., 1992; Menon et al., 1992; Ogawa et al., 1993).

Improving the technology involved in mapping and detection of cerebral oxygenation has many practical applications in both research and clinical diagnosis and treatment.

The problem with oxygen mapping in the cranium stems from the unpredictable and non-uniform way oxygen is distributed and the lack of good measurement systems to image these heterogeneous regions. Oxygen tensions can vary from miniscule amounts to over 70 mm Hg along microscopic tracks in the brain and varies greatly between major structures. These tensions vary greatly during task activation and are abnormal in problem structures such as tumors and stroke

infarcts. Two technologies developed have vastly improved the ability to work around these limitations.

### **1.1 Magnetic Resonance Technology**

The first technology is function MR imaging (fMRI), otherwise known as blood oxygen level dependant imaging (BOLD). According to theory, decreases in local deoxyhemoglobin content cause a decrease in magnetic susceptibility which results in a brightened MR image (Ogawa et al., 1993). The methodology involves magnetic resonance imaging of the brain using specific MR sequences which are sensitive to field inhomogeneities. These sequences are sensitive to deoxyhemoglobin content. Modeling studies and work with phantoms indicate that the relationship between the image intensity and deoxyhemoglobin concentration is predictable if certain key parameters such as sample orientation and magnetic field strength are fixed (Yablonskiy & Haacke, 1994; Dunn & Swartz, 1996; Yablonskiy, 1998). BOLD imaging provides excellent spatial and temporal data but requires careful calibration and, because of the effort and time involved in MR imaging, is not a practical medium for real-time monitoring of oxygenation.

### **1.2 Near Infrared Spectroscopy**

The second technology is near infrared (NIR) spectroscopic diffuse tomography. NIR has been used to quantitatively map hemoglobin concentration and hemoglobin oxygen saturation in tissue-like phantoms as well as determine average values *in vivo*. The methodology involves shining laser light at the head and detecting the scattered light with photomultipliers. This method has been

used in research to monitor brain oxygenation. The light source can be intensity modulated in the hundreds of megahertz range to measure the photon's migration through the tissue which is essentially the average optical pathlength through the tissue. The absorption due hemoglobin in the tissue can be used to determine the blood oxygen level through measurement of amplitude and phase distortions in the light signal. The optical properties of absorption and scattering coefficients are dependent on tissue and wavelength. By recording light signals from many illumination and detection positions and determining the distribution of optical property values required to maintain the observed light signal for each condition, the needed coefficients can be estimated on a spatial scale to form an image. NIR also has the benefit of decreased cost in recent years for advances in optoelectronics. In clinical trials although NIR has been used with some success to detect changes in blood flow and oxygen saturation in a monitoring situation (Rolfe et al., 1992), but these trend monitors have limited use in diagnosis of pre-existing conditions. The main limitation is that it is very difficult to take measurements within highly scattering tissue such as the brain with its non-homogenous distribution of hemoglobin.

### **1.3 Merging of Magnetic Resonance and Spectroscopic Imaging**

Theoretically, a merging of BOLD imaging and NIR detection may yield increased spatial resolution of brain oxygenation as well as an improved quantifiable measurement of oxygenation that can be mapped to specific brain structures. The advantages are that the spatial information from MRI can be used in finite element modeling to increase the spatial resolution of NIR images. The NIR data can also be used to aid in calibration of the MRI results. Unlike

other detection methodologies, the magnetic fields caused by MRI tubes do not affect the accuracy of the NIR measurements so that the two systems are compatible for simultaneous data acquisition. However the development of a combined MRI-NIR imaging system has many engineering challenges as well which need to be addressed for successful system implementation.

#### **1.4 Goals of this thesis**

The two main goals of this thesis project are to improve upon the NIR methods of deriving absorption and scattering coefficients and to begin preliminary work on the melding of NIR and BOLD technology.

The research detailed in this thesis had two distinct stages. The first stage was the development and testing of an automated algorithm in Fortran for fitting measurements of phase shift and amplitude to an analytic diffusion theory expression to derive absorption and scattering coefficients based on an analytic theory. The current method of NIR requires iterative calculations and therefore has an associated time cost. The second stage was preliminary work in combining NIR and BOLD imaging by development and image testing of a MATLAB-based program to turn *a priori* BOLD data sets into finite-element meshes tagged with tissue properties.

The outline for this paper will be as follows. First I will discuss several prior works related to both problems I studied. Then I will discuss my own algorithm and the theory related to it. Next I will describe problems associated with the

system developed. Finally I will discuss results and discuss extensions to both the experimental and theoretical systems.

## **2 Related Work**

The work for this thesis was mainly inspired by prior research in NIR at the Thayer School of Engineering and the Dartmouth Hitchcock Medical Center (DHMC) which has been concentrated on the application of imaging for cancer-detection in the human breast. Concurrently, BOLD images of rat craniums to study artificially-induced tumors has been a concentration of researchers at the Dartmouth Medical School. Use of structural MRI images to enhance NIR images of rat craniums has been a recent adaptation of the breast-imaging study. Extension of this technology of BOLD and NIR imaging for human cerebral oxygen studies is a logical next step.

### **2.1 NIR Breast Imaging**

Near infrared spectroscopy is a noninvasive method sensitive to oxygenation of tissue. Specifically, because the absorption spectra of deoxyhemoglobin and oxyhemoglobin exhibit a marked difference, the hemoglobin oxygen saturation may be determined from the tissue absorption spectrum when reconstructed from appropriate reflectance measurements (Hull et al., 1998). Determination of oxyhemoglobin saturation in the near infrared spectral region depends on the ability to determine the absorption spectrum in the presence of scattering by tissue and the ability to account for particles other than hemoglobin in the measured tissue.

The driving force behind the development of NIR spectroscopy and imaging has been the increase in blood volume within cancerous tumors corresponding to an increase in hemoglobin concentration — estimated to exist at four times contrast with normal tissue. McBride et al., 1998 showed that a series of phantom calibrations could achieve accurate absorption and reduced scattering coefficient images at multiple optical wavelengths. A least squares fit was used to determine hemoglobin concentration and hemoglobin oxygen saturation images from the absorption coefficient images at multiple NIR wavelengths. This methodology was tested both on phantoms composed of intralipid and water with varying hemoglobin concentration and oxygen saturation and in breast tissue *in vivo*.

The breast imaging setup (McBride et al., 1998) consisted of 16 source and 16 detector optical fibers positioned in a circular array. A titanium sapphire laser was used as a light source to pass a laser beam through a source fiber for subsequent detection in each of the 16 detector fibers. The laser was tunable between 700 and 850 nanometers (nm) using a single optical setup). A photomultiplier tube is used for detection within a circuit which allows for detection of the signal amplitude and phase shift at a lower frequency of 1 kHz. Data acquisition, signal processing and instrument control routines were written within the LABVIEW language. The software to perform image reconstruction collects the 256 data points acquired for a single wavelength and reconstitutes them into an image of tissue optical properties consisting of absorption and scattering coefficients using a finite element based calculation of the diffusion equation (McBride et al., 1998). This same hardware and software is not limited

to breast imaging and has been adapted for use with rat craniums and can be further extended.

Light propagation in tissue is approximated by the diffusion equation:

$$-\nabla \cdot D(r)\nabla\Phi(\mathbf{r},\omega) + [\mu_a(\mathbf{r}) + i\omega/c]\Phi(\mathbf{r},\omega) = s_0(\mathbf{r},\omega)$$

where  $\Phi$  is the optical light fluence rate, given at any point  $\mathbf{r}$ , at modulation frequency  $\omega$ , traveling through tissue with optical properties defined by diffusion coefficient  $D$  and absorption coefficient  $\mu_a$  with the speed of light in the medium,  $c$ . The diffusion equation is solved numerically using a finite element (FEM) algorithm (McBride et al., 1998) which I will detail later while describing my new algorithm for faster NIR optical property calculation.

## 2.2 Rat Cranium Studies

Pogue et al., 1999 took NIR measurements of rat craniums and correlated them with corresponding MRI images as a preliminary test of utilization of MRI structure in functional imaging. These experiments utilized the same laser array and equipment previously used for breast imaging was adapted for use with rats.

In these experiments the rats were anesthetized during the procedure and oxygen was varied between low levels of about 10 percent and as high as 90 percent during these tests. A variety of NIR-MRI algorithms were then used to demonstrate the value of inclusion of *a priori* MRI tissue segmentation into the already-existing NIR reconstruction algorithm.

### 3 Methods

The first part of my research involved calibration of NIR tissue spectroscopy for cerebral measurements. The second part was the development software to generate a tagged finite element mesh to integrate *a priori* BOLD information with NIR data.

#### 3.1 Tissue Spectroscopy Calibration — Analytic Infinite-Medium Diffusion

There are various problems associated with NIR measurement in tissue. The method for NIR measurement described in related work processes NIR measurements using a finite-element solution. This solution uses a forward solution of the diffusion equation where the calculating program iteratively fits the computations of measured data to determine the closest tissue optical properties for a homogeneous medium (McBride et al., 1998). The equation involved 40 iterations of this solution and results in an algorithm that has a substantial downtime.

Pogue et al., 1999 compared three methods of frequency-domain measurement processing with a modified Beer-Lambert diffusion law method, an analytic infinite-medium diffusion theory expression and the aforementioned numerical finite element solution which requires iterative processing.

In analytic infinite-medium diffusion theory, the propagation of light is described by radiation transport theory whose simplification results in a diffusion equation that can be solved analytically for simple geometric objects. But this assumes the tissue geometry is regularly shaped. An analytic solution

with multiple source and detector locations, as in the setup used by McBride et al., 1998 in their NIR research, can be used to approximate spatial derivatives of the phase shift and intensity ratio which can fit their analytic counterparts.

For the analytic solver I wrote, the expressions:

$$\frac{d\phi}{d\rho} = \left(\frac{\mu_a}{D}\right)^{\frac{1}{2}} \left[1 + \left(\frac{\omega}{\mu_a c}\right)^2\right]^{\frac{1}{4}} \sin\left[\frac{\tan^{-1}\left(\frac{\omega}{\mu_a c}\right)}{2}\right]$$

$$\frac{d(\ln(\rho I_{AC}))}{d\rho} = \left(\frac{\mu_a}{D}\right)^{\frac{1}{2}} \left[1 + \left(\frac{\omega}{\mu_a c}\right)^2\right]^{\frac{1}{4}} \cos\left[\frac{\tan^{-1}\left(\frac{\omega}{\mu_a c}\right)}{2}\right]$$

were used where  $I_{AC}$  is the AC intensity measured by the detector,  $D$  is the diffusion constant  $D = (3\mu_a\mu_s')^{-1}$  where  $\mu_a$  is the absorption coefficient and  $\mu_s'$  is the derivative of the scattering coefficient,  $\rho$  is the chord distance between source and detector. These expressions are matched to measurements of phase shift versus distance and  $\ln(\rho I_{AC})$  versus distance to derive  $\mu_a$  and  $\mu_s'$  values (Pogue et al., 1999).

### 3.2 Finite Element Mesh

Using the MATLAB programming environment, for ease of image manipulation, I wrote a utility program which can be utilized almost immediately with BOLD images to create a heterogeneous finite element mesh to improve the overall reconstruction quality of an NIR image using appropriate tissue values. This is an extension of the previous tests combining MRI and NIR data because the

mesh derivation tool is intended for use with BOLD data corresponding to the subject being tested: in this case a rat with an (unfortunately small) artificially-induced tumor. These tumors could be seen in the resulting BOLD image and, in theory, the BOLD image can be used to enhance NIR spectroscopy to an extent that the tumor will show up in a combined updated image.

### **3.3 Actual Trials**

It was my hope that the tools I developed for my thesis would be tested on rats with artificially-induced tumors as well as clinically at DHMC on healthy infants as a precursor to pre-term infant testing and monitoring of brain oxygenation. Unfortunately these trials did not pan out and remain needed tests of the software written.

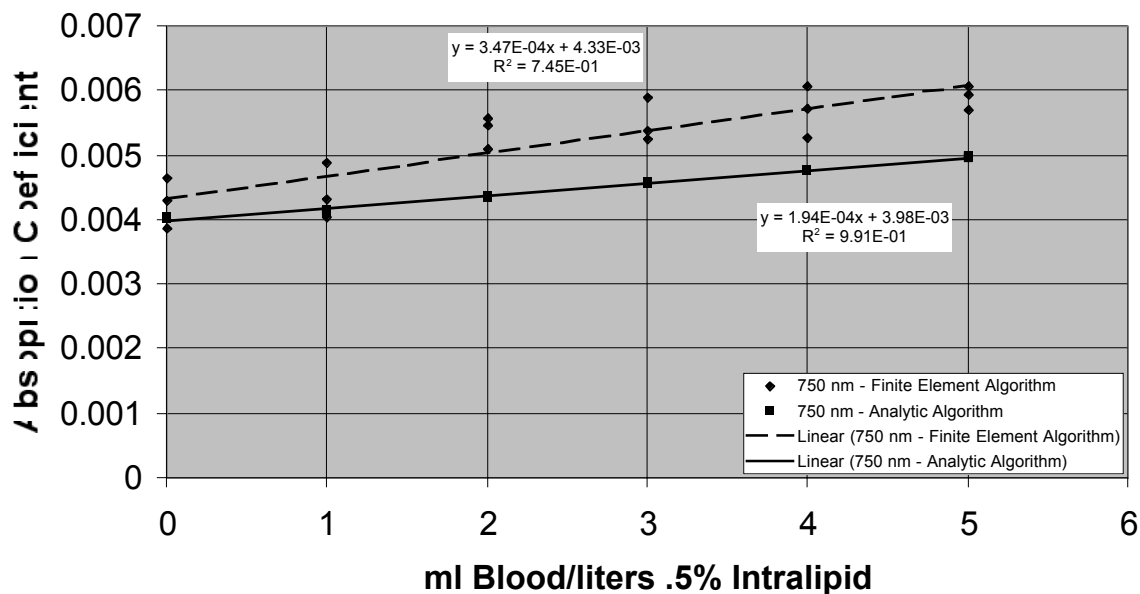
## **4 Results and Discussion**

### **4.1 Analytic Infinite-Medium Diffusion for Tissue Spectroscopy**

My NIR analytic algorithm was tested on the same NIR data set as the original iterative finite element algorithm and the resulting diffusion expression and data analysis can be seen in figure 1. The main medium for comparison between the two calculation methods is through the extinction coefficient. Wray et al., 1988 characterized the extinction coefficient of the phantoms examined for figure 1 at  $3.12 \times 10^{-4} \text{ [(ml/L)}^{-1}\text{mm}^{-1}]$ . The calculated extinction coefficient for the two methods of data analysis can be derived from the slope of the linear regression lines.

Figure 1: Analytic vs. Finite Element

### Comparison of Measured Absorption Methods



Comparison with prior theoretical and actual observed extinction coefficients with regards to the absorption coefficient versus blood amounts demonstrates that although the finite element algorithm demonstrates a large point-to-point error margin, its final linear regression is closer to the actual absorption coefficient of the tested phantom. The analytic algorithm comes close in terms of matching the actual absorption coefficient and extinction coefficient but has more error as volume of blood and intralipid increases.

This result demonstrates the problems inherent in the infinite-medium assumptions of the analytic algorithm utilized in my program. The finite element solution to the diffusion equation possibly has similar problems but resolves them during the course of the 40-step iterative calculation process to

match solutions with actual data. A possible use of my analytic solution, which is close but less accurate, is as a possible first-guess mechanism for a more complex solution set that requires more time.

Figures 2 through 5 show the results of using my analytic solver as a first guess for the finite element calculating program developed by McBride et al., 1998. This is contrasted against an initial 'bad guess' which iteratively throws the solution off track for as many as 40 iterations. This is especially evident in the error analysis of intensity and phase fit iterations in figures 4 and 5. The analytic solution may not be the most accurate solution but its speed makes it practical for derivations of better solutions or for a quick analysis of the NIR data.

Figure 2

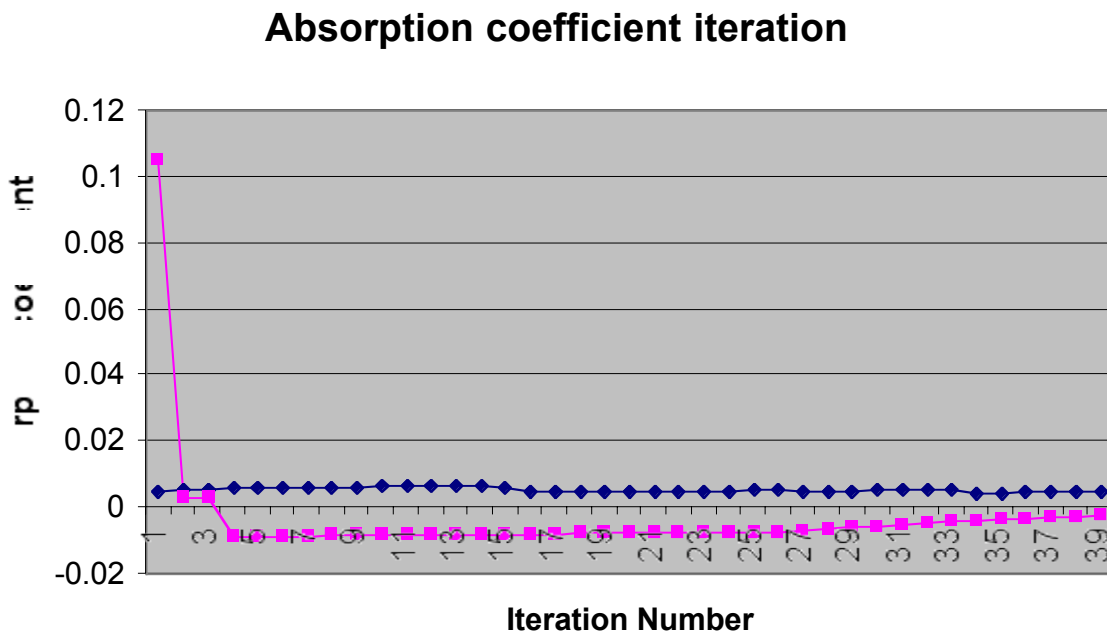


Figure 3

### Scattering coefficient iteration

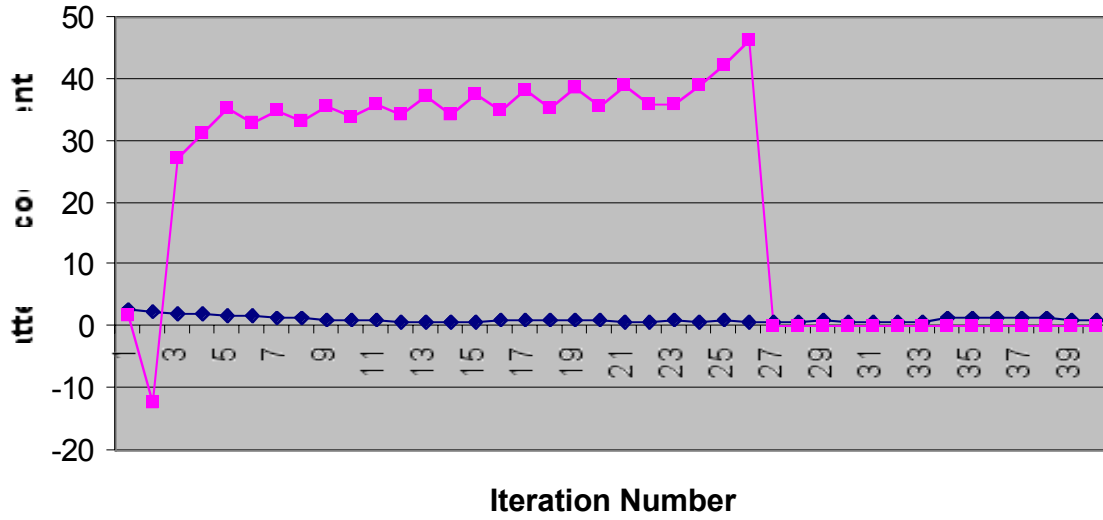


Figure 4

### Intensity fit iteration

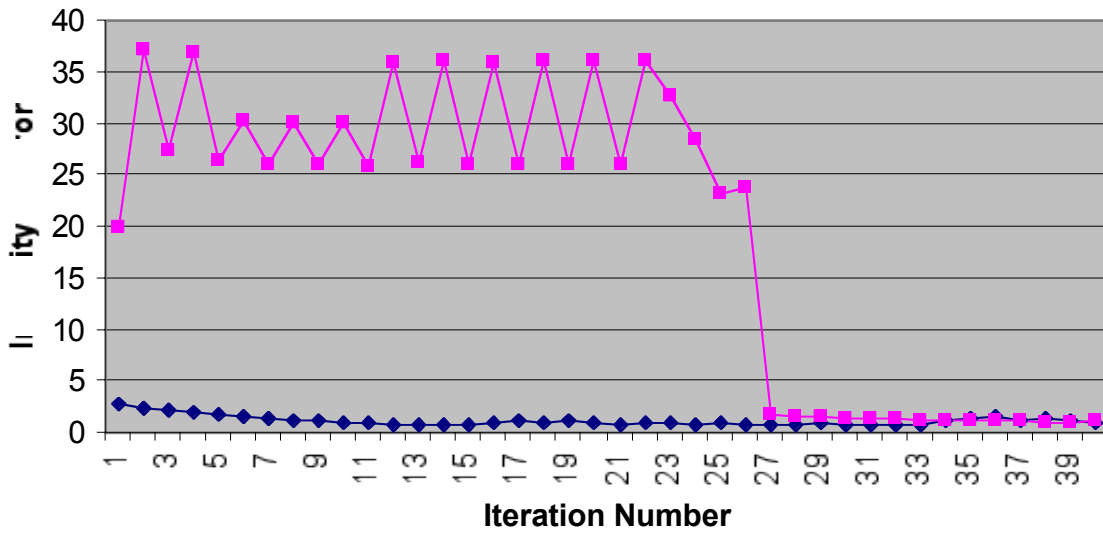
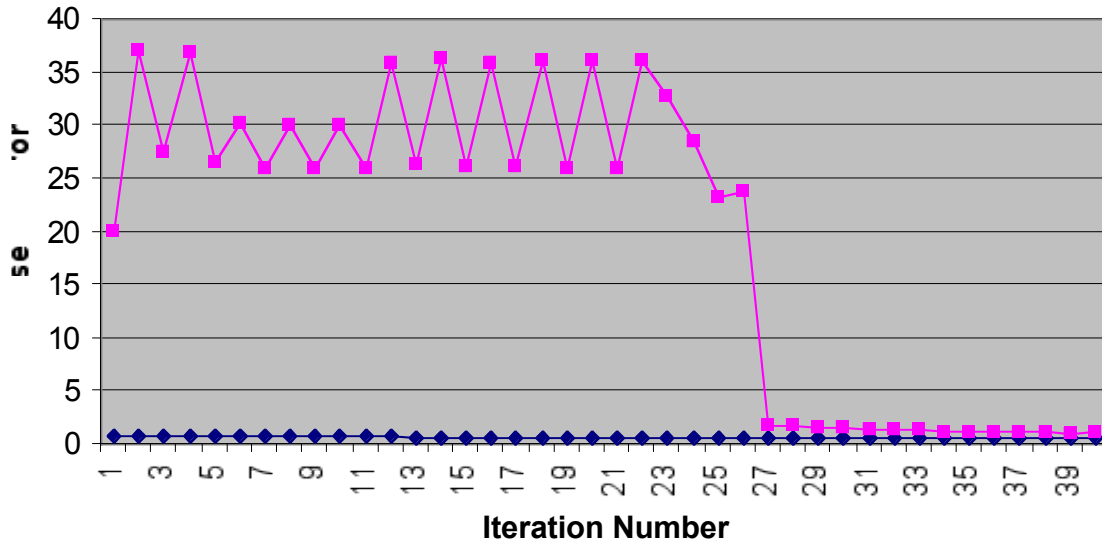


Figure 5

### Phase fit iteration



#### 4.2 Material Tagging from BOLD images

Compared to the analytic diffusion work, the finite element mesh generated from *a priori* BOLD images is relatively simple using the tools available in the MATLAB programming environment. MATLAB has several toolboxes built in for image manipulation — in this case the MRI images were saved as ‘tiff’ files — as well as edge detection, mesh generation and material property tagging.

The program I wrote relies heavily on user-feedback to generate the optimal mesh for the specific image being studied. Figures 6 through 11 show a sample image of a rat at 21% oxygen tagged using my finite element mesh generator.

**Figure 6: Original BOLD image**

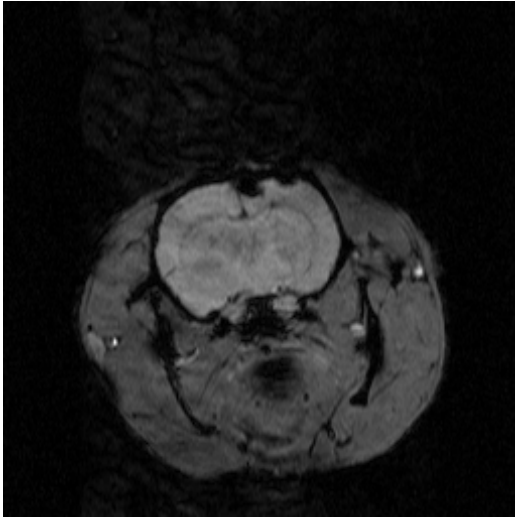


**Figure 7: Threshold Image**

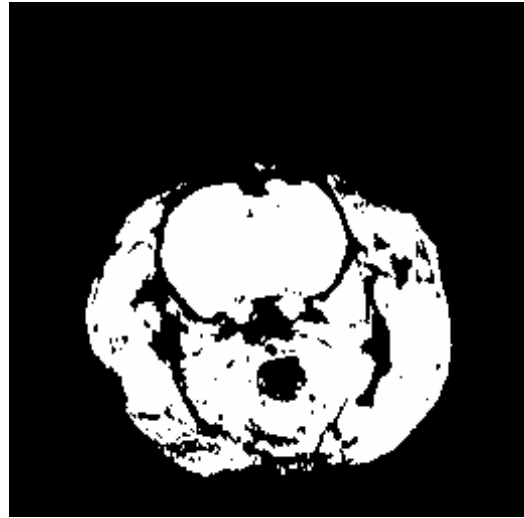
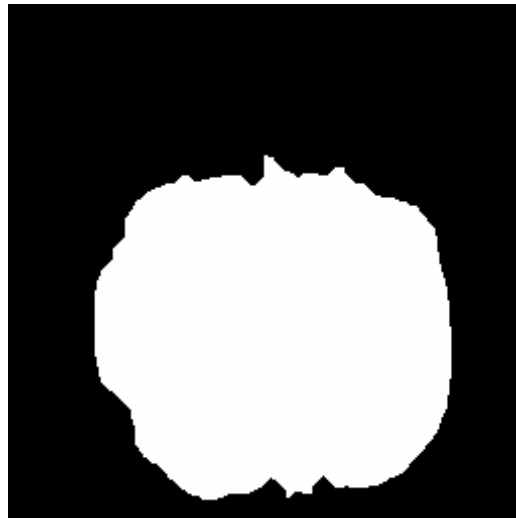


**Figure 8: Processed Image**



In figures 6 through 8, the BOLD image is converted into a simple black and white image with image thresholding. Intercranial structures, such as bone and the spinal column, which are interpreted by the computer as black are filled in to create a homogeneous solid representative of the actual cranium being studied.

Figures 9 and 10 show the next steps: edge detection and generation of the finite element mesh.

**Figure 9: Edge Detection**

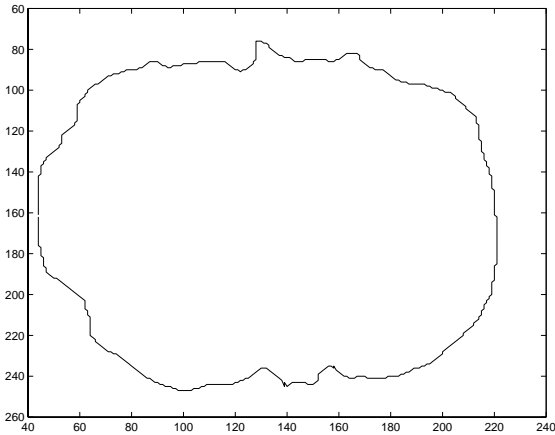


**Figure 10: Finite Element Mesh**

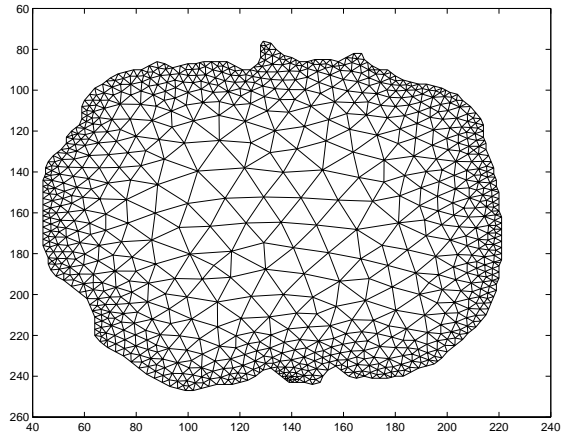
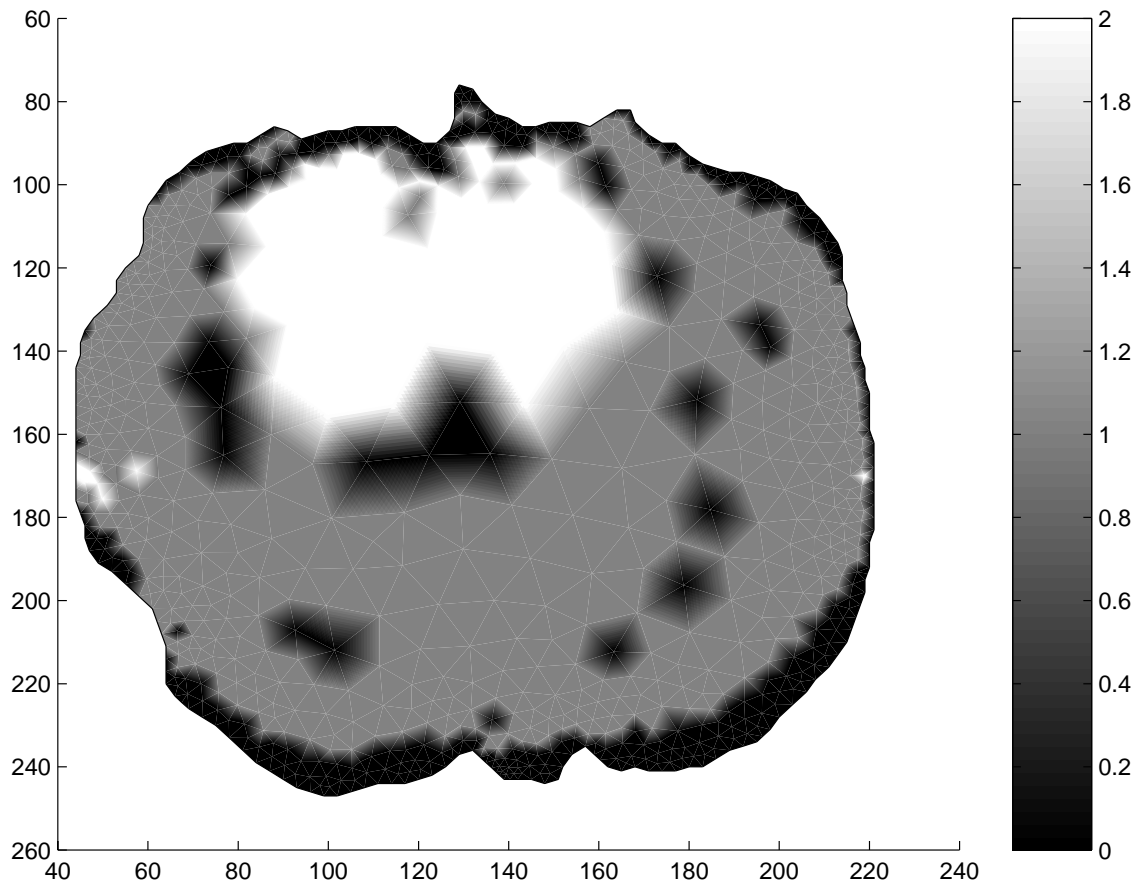
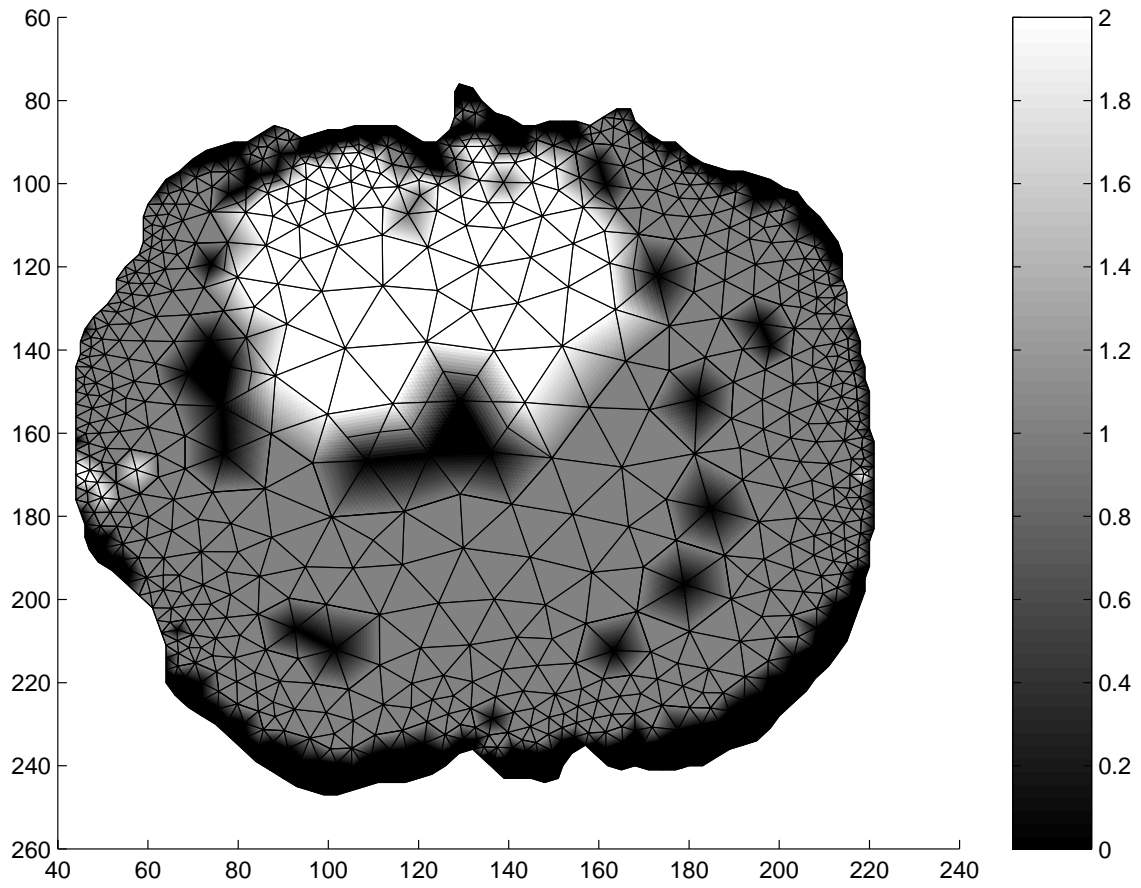


Figure 11 shows the resulting material-tagged meshes. These meshes have been separated into three materials: brain, bone and muscle. It is conceivable that in the future more structures will be incorporated and the code easily supports such an addition. Currently these structures have pre-defined experimentally determined diffusion properties which merely aid in NIR measurements but future extension of the combination of NIR and BOLD can utilize the mesh to maintain updated oxygenation information.

Figure 11: Material Tagged Meshes



## **5 Extensions**

Obviously a great deal more research and work needs to be done before the ultimate goal of utilizing MRI and NIR together for oxygen detection and mapping is realized. My original thesis proposal involved further testing on multiple rat subjects — all with artificially induced tumors — to calibrate the detection properties of NIR and BOLD with regards to detecting brain abnormalities. Unfortunately, the rat subject with the tumor died in a preliminary BOLD scan while in the MRI tube. Other rats failed to have the tumor take. This remains a needed study and will be a valid test of the software I have written.

A more ambitious study initially planned involved NIR calibration and monitoring of healthy infants at DHMC. The eventual goal would be the utilization of NIR and BOLD to monitor pre-term infants. I co-wrote a Committee for the Protection of Human Subjects (CPHS) protocol that was submitted to DHMC but has yet to be approved. The current breast-imaging array provides the basis for this study to be carried to fruition in the near future.

## **6 Acknowledgments**

This thesis project would have been impossible without the help, support and advice from advisors Brian Pogue, Keith Paulsen and George Cybenko. I would especially like to thank Professor Pogue and Troy McBride for their time spent guiding me through the various stages of the research and for the many hours spent developing much of the crucial background for my current work.

## 7 References

P. Bandettini, E. Wong, R. Hinks, L. Estowski, J. Hyde, "Quantification of changes in relaxation rates  $R2^*$  and  $R2$  in activated tissue" (1992)

K.K. Kwong, J.W. Belliveau, D.A. Chesler, I.E. Goldberg, R.M. Weisskoff, et al., "Dynamic magnetic resonance imaging of human brain activity during primary sensory stimulation" (1992)

R.S. Menon, S. Ogawa, S. Kim, J.M. Ellermann, H. Merkle, D.W. Tank, K. Ugurbil, "Functional brain mapping using magnetic resonance imaging: signal changes accompanying visual stimulation" (1992)

J.F. Dunn, H.M. Swartz, "Blood oxygenation: heterogeneity of hypoxic tissues monitored using bold MR imaging" (1996)

D.A. Yablonskiy "Quantitation of intrinsic magnetic susceptibility-related effects in a tissue matrix. Phantom study." (1998)

D.A. Yablonskiy, E.M. Haacke "Theory of NMR signal behavior in magnetically inhomogeneous tissues: the static dephasing regime" (1994)

P. Rolfe, Y.A. Wickramasinghe, M.S. Thorniley, et al. "Fetal and neonatal cerebral oxygen monitoring with NIRS: theory and practice" (1992)

E.L. Hull, D.L. Conover, T.H. Foster, "Carbogen-Induced Changes in Rat Mammary Tumor Oxygenation Reported By Near Infrared Spectroscopy" (1998)

T. McBride, B. Pogue, E. Gerety, S. Poplack, U. Osterberg, K. Paulsen, "Spectroscopic Diffuse Optical Tomography for Quantitatively Assessing Hemoglobin Concentration and Oxygen Saturation in Breast Tissue" (1998)

B. Pogue, K. Paulsen, C. Abele, H. Kaufman, "Calibration of Near Infrared Frequency-Domain Tissue Spectroscopy for Absolute Absorption Coefficient Quantitation in Neonatal Head-Simulating Phantoms" (1999)

B. Pogue, T. McBride, C. Nwaigwe, U. Osterberg, J. Dunn, K. Paulsen, "Near-infrared diffuse tomography with *a priori* MRI structural information: testing a hybrid image reconstruction methodology with functional imaging of rat cranium" (1999)

B. Pogue, K. Paulsen, "High-resolution near-infrared tomographic imaging simulations of the rat cranium by use of *a priori* magnetic resonance imaging structural information" (1998)

S. Wray, M. Cope, D.T. Delpy, J.S. Wyatt, and E.O.R. Reynolds, "Characterization of the near infrared absorption spectra of cytochrome aa<sub>3</sub> and haemoglobin for the non-invasive monitoring of cerebral oxygenation" (1988)

## Appendix A — Analytic Diffusion Fitting Algorithm

```
c    nirfit.for

c    #####
c    # Program to fit phase and Ln(rIAC) slopes
c    # using NIR data with varying r values
c    # from chords around non-circular data area
c    # UNIX compile line: f77 -g nirfit.for -o nirfit

c    # Written David Kung '99
c    # on 2/99 based on phinfit.for program
c    # written by Brian Pogue

PROGRAM NIRFIT

c    # variables
character *64 dfname, sfile1, sfile2
double precision rData(1:16), iData(1:16), diam
real srcX(1:16), srcY(1:16), detX(1:16), detY(1:16)

double precision Iac(1:16), R1(1:16), phi(1:16), lnrIac(1:16)
double precision m0, mi

c    Declare functions
DOUBLE PRECISION FIT

c    # files to open (commented defaults)
c    dfname = 'd:\labview\autoimag\nov98\no208g1.asc'

sfile1 = 'd:\recon\16_S_loc.nod'
sfile2 = 'd:\recon\16_D_loc.nod'

print *, 'Input data file name... '
read (*,8) dfname
08    format(a)
print*, 'What is the diameter of the cylinder (default=86) ?'
read*, diam
IF (diam.eq.0.0) diam=86.0
c    print *, 'Input source file name...'
c    read *, sfile1
c    print *, 'Input detector file name...'
c    read *, sfile2
print *
print *
print *, 'Opening:', dfname, sfile1, sfile2

c    # load file data

call loadData(rData, iData, dfname, 16)
print*, 'data OK'
c    print *, 'Before loadUnit'
c    do 10 k = 1, 16, 1
c        print *, k, ':Real:', rData(k)
c        print *, ':Imag:', iData(k)
```

```

c 10  continue
c     print *

c     # load source/detector
c     call loadUnit(srcX, srcY, sfile1, 16)
c     print*, 'sources OK'
c     call loadUnit(detX, detY, sfile2, 16)
c     print*, 'detectors OK'

c     print *, 'After loadUnit'
c     do 11 k = 1, 16, 1
c         print *, k, ':Real:', rData(k)
c         print *, ':Imag:', iData(k)
c 11  continue
c     print *

c     print *, 'Source/Detectors'
c     do 12 k = 1, 16, 1
c         print *, k, ':S:', srcX(k), srcY(k), ':D:', detX(k), detY(k)
c 12  continue
c     print *

c     ##### Data Loaded #####

c     # Iac value, chord, phi

c     srcX(1)=srcX(1)/86.0*diam
c     srcY(1)=srcY(1)/86.0*diam
c     do 20 k = 1, 16, 1
c         Iac(k) = (rData(k)**2 + iData(k)**2)**0.5
c         detX(k)=detX(k)/86.0*diam
c         detY(k)=detY(k)/86.0*diam
c         R1(k) = ((srcX(1) - detX(k))**2 + (srcY(1) - detY(k))**2)**0.5
c         phi(k) = atan(iData(k)/rData(k))*180./3.14159
c         lnrIac(k) = log(R1(k)*Iac(k))

20  continue

c     do 21 k = 1, 16, 1
c         print *, k, ' Iac', Iac(k)
21  continue

c     do 22 k = 1, 16, 1
c         print *, k, ' R1', R1(k)
22  continue

c     do 23 k = 1, 16, 1
c         print *, k, ' Phi', phi(k)
23  continue

c     do 24 k = 1, 16, 1
c         print *, k, ' ln(rIac)', lnrIac(k)
24  continue

c     m0 = FIT (R1, phi, 16)
c     mi = FIT (R1, lnrIac, 16)

```

```

print *, 'Phi-Fit:', m0
print *, 'ln(rIac)-Fit:', mi
print *

call phinfit (mi, m0)

STOP

END

c #####
c # loadData
c # Subroutine to grab real/imag data from file
c # This subroutine grabs the real and imaginary data
c # from the file

SUBROUTINE loadData(rData, iData, dfname, Length)

character*64 dfname
real unum
double precision rData(1:Length), iData(1:Length)

open (unit = 110, file = dfname, status = 'old')

rewind (110)

do 120 j = 1, Length, 1

    READ (110, *, END=120) unum, iData(j)
    READ (110, *, END=120) unum, rData(j)

120 continue

close (unit = 110)

c    print *, 'Inside Subroutine'
c    do 130 j = 1, Length, 1
c        print *, j, ':Real:', rData(j)
c        print *, ':Imag:', iData(j)
c 130 continue
c    print *

RETURN

END

c #####
c # loadUnit
c # Subroutine to grab source/detector x&y locations

SUBROUTINE loadUnit(X, Y, fname, Length)

character*64 fname
real unum
real X(1:Length), Y(1:Length)

```

```

open (unit = 210, file = fname, status = 'old')

do 220 m = 1, Length, 1
  READ (210, *, END=220) unum, X(m), Y(m)

220 continue

close (unit = 210)
RETURN

END

c #####
c # function fit
c # Function to find best fit line given
c # set of x and y data points

DOUBLE PRECISION FUNCTION FIT (x, y, Length)

double precision x(1:Length), y(1:Length)
double precision delta, sumXsq, sumY, sumX, sumXY
double precision B

sumX = 0
sumY = 0
sumXsq = 0
sumXY = 0
B = 0
fit = 0

do 310 j = 1, Length, 1
  sumX = sumX + x(j)
  sumY = sumY + y(j)
  sumXsq = sumXsq + (x(j))**2
  sumXY = sumXY + (x(j)*y(j))
310 continue

c   print *, 'SumX:', sumX
c   print *, 'SumY:', sumY
c   print *, 'SumXsq:', sumXsq
c   print *, 'SumXY:', sumXY

delta = (Length * sumXsq) - sumX**2

c   print *, 'Delta:', delta

B = ((Length*sumXY)-(sumX*sumY))/delta

c   print *, 'fit:', B

FIT = B

return
end

c #####

```

```

c   # phinfit
c   # Code written by Brian Pogue
c   # Adapted for line-fitting

SUBROUTINE phinfit (a1, p1)

double precision a1, p1
double precision w,c,ua,us,f1,alpha,phi
integer nn(600)

w=1.0e8*2.0*3.14159
c=3.0e11/1.333
ua=0.01
us=.5
D=1/(3*(ua+us))

print*, 'Phinfit Region'
print*
c   print*, a1,p1
p1=abs(p1)

c   do 1010 j=1,5

f1=((ua**2+(w/c)**2)/(D**2))**.25
alpha=-f1*cos(0.5*atan(w/c/ua))
phi=f1*sin(0.5*atan(w/c/ua))*180/3.14159

c   print*, ua,alpha,phi
c   print 1500, ua,us,alpha,phi,a1,p1

do 1000 i=1,25
f1=((ua**2+(w/c)**2)/(D**2))**.25
alpha=-f1*cos(0.5*atan(w/c/ua))
phi=f1*sin(0.5*atan(w/c/ua))*180/3.14159

ua=ua+0.0001
D=1/(3*(ua+us))
f1=((ua**2+(w/c)**2)/(D**2))**.25
alpha1=-f1*cos(0.5*atan(w/c/ua))
phi1=f1*sin(0.5*atan(w/c/ua))*180/3.14159
ua=ua-0.0001
da=(alpha-alpha1)/0.0001
ds=(phi-phi1)/0.0001
ua=ua-(a1-alpha)/da
us=us-(p1-phi)/ds*.1
D=1/(3*(ua+us))
f1=((ua**2+(w/c)**2)/(D**2))**.25
alpha=-f1*cos(0.5*atan(w/c/ua))
phi=f1*sin(0.5*atan(w/c/ua))*180/3.14159
c   print 1500, ua,us,alpha,phi,a1,p1

us=us+.001
D=1/(3*(ua+us))
f1=((ua**2+(w/c)**2)/(D**2))**.25
alpha2=-f1*cos(0.5*atan(w/c/ua))
phi2=f1*sin(0.5*atan(w/c/ua))*180/3.14159

```

```

da=(alpha-alpha2)/0.001
ds=(phi-phi2)/0.001
us=us-0.001
ua=ua-(a1-alpha)/da*.01
us=us-(p1-phi)/ds*.2
D=1/(3*(ua+us))
f1=((ua**2+(w/c)**2)/(D**2))**.25
alpha=-f1*cos(0.5*atan(w/c/ua))
phi=f1*sin(0.5*atan(w/c/ua))*180/3.14159
print 1500, ua,us,alpha,phi,a1,p1

1000  continue
      print*, ' '
      print*, 'best fit absorption and scattering coeffs.'
      print 1500, ua,us
      write (11,1510) ua, us

1010  continue

1500  format (f10.5,f10.5,f10.4,f10.4,f10.4,f10.4)
1510  format (f10.5,f10.5)

      RETURN
      END

```

## Appendix B — Finite Element Mesh Code

```
% bmesh.m

% David Kung '99
% Rat imaging, thresholding and tagging program
% Spring, 1999

% Clear all
clear all;
close all;

% Read in file

file = input ('Filename to open? ','s');
gray = imread (file);

imshow (gray);

% Determine threshold discrimination

okay = 'y';
while (okay ~= 'n'),
    threshold = input ('What is your desired threshold value (Btw 0 and
1)? ');
    bw = im2bw (gray, threshold);
    imshow (bw);
    okay = input ('Do you want to re-input threshold (y/n)? ', 's');
end

% Create solid tissue object

okay = 'n';
times = 0;
solid = bw;
input ('We will now fill in the tissue voids to create solid tissue
object (hit enter)');
while (okay ~= 'y'),
    SE = ones(6,2);
    solid = dilate (solid,SE);
    imshow(solid);
    times = times + 1;
    okay = input ('Are you satisfied with the amount of fill-in? (y/n)
', 's');

end

for i = 1:1:times,
    solid = erode(solid);
end

imshow (solid);

% Edge
input ('Edge detection (press enter)');
ed = edge(solid);
```

```

imshow (ed);

% Discern Edge Coordinates

f = 1;
for x = 1:1:size(ed,1),
    for y = 1:1:size(ed,2),
        if (ed(y,x) > 0)
            xy(f, 1) = x;
            xy(f, 2) = y;
            f = f+1;
        end;
    end;
end;

Max = max(xy);
Xmax = Max(1)/2;
Ymax = Max(2)/2;
Min = min(xy);
Xmin = Min(1)/2;
Ymin = Min(2)/2;

for x = 1:1:size(xy,1),
    xyT(x,1) = xy(x,1)-Xmax-Xmin;
    xyT(x,2) = xy(x,2)-Ymax-Ymin;
end;

% Tangent angle sorting

for x = 1:1:size(xyT,1),
    theta = atan2(xyT(x,2),xyT(x,1));
    xyA(x, 1) = theta;
    xyA(x, 2) = xyT(x,1);
    xyA(x, 3) = xyT(x,2);
end;

xyA = sortrows (xyA,1);

% Restoring centering
for x = 1:1:size(xyA,1),
    xyA(x,2) = xyA(x,2)+Xmax+Xmin;
    xyA(x,3) = xyA(x,3)+Ymax+Ymin;
end;

input ('Sorted semi-circular plot (press enter)');

plot (xyA(:,2),xyA(:,3));
axis ij

% Remove every fifth element (for size sake) - ~550 points down to ~180

for x = 3:3:size(xyA,1),
    xyFin(x/3,1) = xyA(x,2);
    xyFin(x/3,2) = xyA(x,3);
end;

pdepoly (xyFin(:,1)',xyFin(:,2)');

```

```

% Wait for pde to finish

input ('Done creating and exporting mesh? (press enter)');

% Material Properties Needs:
%
% Ability for user
to threshold

input ('Now to add material properties. (press enter)');

    for x= 1:1:size(p,2),
        node(x,1) = x;
        node(x,2) = p(1,x);
        node(x,3) = p(2,x);
    end;

for i = 1:1:size(node,1),
    x = round(node(i,2));
    y = round(node(i,3));

    shade = gray(y,x);

    material2(i,1) = i;

    if (shade<30)
        % black
        material2(i,2) = 0;
    elseif (shade<95)
        % mid
        material2(i,2) = 1;
    else
        % light
        material2(i,2) = 2;
    end;

end;

for i = 1:1:size(material2,1),
    mat(i,1) = material2(i,2);
end;

pdeplot(p,e,t,'xydata',mat,'mesh','off','colorbar','on','contour','on',
'levels',0);
axis ij
colormap ('gray')

okay = 'n';
okay = input ('Do you want to save mesh information (y/n)? ', 's');

if (okay == 'y')

    dlmwrite ('edgedat.bm',xyFin);

    dlmwrite ('nodes.bm',node);

```

```

for x = 1:1:size(e,2),
    edge(x,1) = x;
    edge(x,2) = e(1,x);
    edge(x,3) = e(2,x);
    edge(x,4) = e(3,x);
    edge(x,5) = e(4,x);
    edge(x,6) = e(5,x);
    edge(x,7) = e(6,x);
    edge(x,8) = e(7,x);
end;

dlmwrite ('edges.bm',edge);

for x = 1:1:size(t,2),
    elt(x,1) = x;
    elt(x,2) = t(1,x);
    elt(x,3) = t(2,x);
    elt(x,4) = t(3,x);
end;

dlmwrite ('elt.bm',elt);

dlmwrite ('material.bm',material2);
end;

```